Diagn Interv Radiol 2023; DOI: 10.4274/dir.2023.232262

INTERVENTIONAL RADIOLOGY

ORIGINAL ARTICLE

Artifact characterization of Nitinol needles in magnetic resonance imaging-guided musculoskeletal interventions at 3.0 tesla: a phantom study

Vanessa Franziska Schmidt
Olaf Dietrich
Max Seidensticker
Moritz Wildgruber
Bernd Erber
Jens Ricke
Sophia Samira Goller

PURPOSE

To characterize the artifacts of an 18-gauge coaxial nickel-titanium needle using a balanced steady-state free precession sequence in magnetic resonance imaging-guided interventions at 3.0 tesla.

METHODS

The influence of flip angle (FA), bandwidth, matrix, slice thickness (ST), and read-out direction on needle artifact behavior was investigated for different intervention angles (IA). Artifact diameters were rated at predefined positions. Subgroup differences were assessed using Bonferroni-corrected non-parametric tests and correlations between continuous variables were expressed using the Bravais–Pearson coefficient. Interrater reliability was quantified using intraclass correlation coefficients (ICCs), and a contrast-enhanced target lesion to non-enhanced muscle tissue contrast ratio was quantified.

RESULTS

The artifact diameters decreased with an increase in FA for all IAs ($P < 0.001$) and with an increase in ST for IAs of 45°–90° (all $P < 0.05$). Tip artifacts occurred at low IAs (0°–45°) and gradually increased in size with a decrease in IA ($P = 0.022$). The interrater reliability was high (ICC: 0.994–0.999). The contrast-enhanced target lesion to non-enhanced muscle tissue contrast ratio presented positive correlations with increasing FAs and matrices ($P < 0.001$; $P = 0.003$) and a negative correlation with increasing STs ($P = 0.007$).

CONCLUSION

To minimize needle artifacts, it is recommended to use FAs of 40°–60°, a ST of >7 mm, and, if possible, an IA of 45°–60°. The visibility of the target lesion and the needle's artifact behavior must be weighed up against each other when choosing the ST, while higher FAs (40°–60°) and matrices (224 × 224/256 × 256) are associated with low artifacts and sufficient lesion visibility.

KEYWORDS

Artifact, interventional, MSK, musculoskeletal, real-time sequence

From the Department of Radiology (V.F.S. ✉vanessa.schmidt@med.uni-muenchen.de, O.D., M.S., M.W., B.E., J.R., S.S.G.), University Hospital, LMU Munich, Munich, Germany.

Received 19 April 2023; revision requested 23 May 2023; last revision received 06 June 2023; accepted 11 June 2023.

Epub: 18.08.2023

Publication date: 05.09.2023

DOI: 10.4274/dir.2023.232262

Magnetic resonance imaging (MRI) encompasses excellent characteristics for the image guidance of interstitial interventional procedures, including a lack of ionizing radiation, high soft tissue contrast, and multiplanar needle guidance with quasi-simultaneous acquisition of two or three orthogonal, oblique slices in near real-time.[1-8] In practice, MRI-guided interventions are performed in clinical routines involving a wide range of body regions with a primary focus on the tissues of organs for which MRI is superior to other imaging modalities, such as the liver, prostate, breast, or spine.[6,8-14] However, interventions of peripheral joints for, for example, the purpose of biopsy extraction, are still most likely to be ultrasound-guided, with MRI-guidance of musculoskeletal interventions beyond the spine rarely performed. Nevertheless, there exist a number of approaches that have trialed real-time dynamic MRI in the field of musculoskeletal imaging. For example, Bayer et al.[15] demonstrated that dynamic visualization of the finger anatomy during a full range of motion can be ob-

You may cite this article as: Schmidt VF, Dietrich O, Seidensticker M, et al. Artifact characterization of Nitinol needles in magnetic resonance imaging-guided musculoskeletal interventions at 3.0 tesla: a phantom study. *Diagn Interv Radiol.* 2023;29(5):719-732.

tained by using a balanced steady-state free precession (bSSFP) sequence.

To be MR-compatible and to ensure a safe procedure for the patient and the performing interventionalist, biopsy needles are made of alloys that cause minimal interference with the outer magnetic field, such as nickel-titanium (Nickel Titanium Naval Ordnance Laboratory; Nitinol), titanium, glass fiber, or steel.[16] However, needle artifacts, which mostly present as low intensity signals in the region around the needle's shaft or tip, cannot be completely excluded and can impair accurate visualization of both the needle and the needle-to-target distance. To successfully perform MRI-guided interventions with reliable target localization for musculoskeletal issues at 3.0 tesla (T) units, a thorough understanding of needle artifact behavior is crucial, regardless of the intended biopsy site. The artifact size is influenced by different parameters, which are either related to the individual composition of the needle, such as the alloy, the diameter, and the length, or, to different MRI-related parameters, such as the orientation of the intervention angle (IA) in relation to the static magnetic field (B_0), the strength of the B_0 field, or the pulse sequence type.[5,10,17-22] Therefore, it is important to reassess the technical and methodological fundamentals of musculoskeletal MRI-guided interventions at 3.0 T. This is, on the one hand, because 3.0 T interventional MRI is more demanding in terms of safety and artifact behavior than interventions at lower fields (e.g., at 1.5 T) and on the other hand, because it can provide rewarding superior image quality when considering important aspects in acquisition parameter selections.

Main points

- The use of a flip angle (FA) of 40°–60° and a slice thickness (ST) of 10–17 mm minimized the needle artifacts while maintaining the best possible visualization of the coaxial intervention needle in this musculoskeletal phantom study at 3.0 tesla. To find a compromise, since the ST should not be set too thick to ensure accurate needle placement during the procedure, we ultimately recommend an ST of >7 mm in clinical practice.
- In addition, if possible, the intervention angles should be 45°–60° to specifically avoid tip artifacts.
- The visibility of the target lesion and the artifact behavior of the intervention needle must be weighed up against each other when choosing the ST, while higher FAs (40°–60°) and matrices (224 × 224/256 × 256) were associated with both low needle artifacts and sufficient target lesion visibility.

This paper presents a systematic investigation of the artifact behavior of an 18-gauge (G) commercially coaxial Nitinol needle as a function of the IA and sequence parameter variations using a bSSFP sequence in a muscle phantom model at 3.0 T. The study aims to characterize artifact formation during clinical MRI-guided high-field interstitial interventions, providing valuable guidance for musculoskeletal tissue biopsies.

Methods

Image acquisition

The MRI process was performed using a closed-bore 3.0 T unit (MAGNETOM Vida, Siemens Healthineers, Erlangen, Germany) with a system length (cover-to-cover) of 186 cm and a bore diameter of 70 cm. The gradient system had a maximum gradient strength of 60 mT/m and a slew rate of 200 T/m/s. The MRI protocol was based on an interventional real-time fluoroscopic bSSFP pulse sequence with true fast imaging with steady-state free precession (TrueFISP) contrast ("Needle Intervention Add-in" package, Siemens Healthineers, Erlangen, Germany). This pulse sequence allows for visual real-time updates and interactive graphical modification of the slice geometry during imaging. A four-channel flex coil (Siemens Healthineers, Erlangen, Germany) with a weight of 550 g (516 × 224 mm) was used as the receive coil.

Ethics committee approval was waived for this study due to the exclusively experimental study design without any animals or patients being involved.

Bovine muscle phantom model

A bovine muscle phantom model with a weight of 5.925 kg, a length of 33 cm, a width of 24 cm, a height of 13 cm, and a maximum transverse diameter of 53 cm was used. As expected, the bovine muscle phantom model had an MRI signal intensity comparable to that of human skeletal muscle. The complete scan series could be performed using the same model, ensuring comparability of the results. Before placing the needles, 0.5 mL of 1.0 mmol/mL gadolinium (Gadovist®, Bayer AG, Leverkusen, Germany) diluted at 1:1000 in 0.9% sodium-chloride (B. Braun, Melsungen, Germany) was applied in a 1.0-mL syringe (B. Braun, Melsungen, Germany) centrally into the muscle phantom by using a 20-G Nitinol needle (ITP, Innovative Tomography Products GmbH, Bochum, Germany) to simulate a contrast-enhanced target lesion at the center of the muscle tissue specimen. Thereafter, a total of seven MR-compatible coaxial Nitinol needles (as described below) were positioned at 0°, 15°, 30°, 45°, 60°, 70°, and 90° relative to the B_0 field using the "entry and target points function" within the real-time fluoroscopic MRI software to guarantee an exact and parallel position of the needles in the B_0 field (2° accepted deviation). The experimental setup is shown in Figure 1.

Magnetic resonance-compatible intervention needle

A commercially available MR-compatible coaxial Nitinol needle (ITP, Innovative Tomography Products GmbH, Bochum, Germany) with a size of 18G (outer diameter: 1.25 mm, length: 150 mm, standardized facet cut) was investigated.

Scan series

The phantom was positioned in the isocenter of the *XZ* plane using the light visor of the MR tomograph. The influence of the following five parameters was investigated as a function of the IA on artifact formation: flip angle (FA), receiver bandwidth (BW), matrix, slice thickness (ST), and read-out direction. The IA (the needle angle relative to the B_0 field) varied from 0°–90° (0°, 15°, 30°, 45°, 60°, 75°, and 90°). As one parameter was modified, the others remained constant with the following predefined settings. The matrix was fixed to 128 × 128 voxels, which was a compromise between acquisition time and spatial resolution. Echo time (TE) and repetition time (TR), which yield an influence on acquisition time, were set to a minimum (TE: 1.71 ms, TR: 3.42 ms) as fixed parameters, resulting in an acquisition time of 461 ms per plane. The field of view was uniformly set to 300 × 300 mm^2. The predefined setting was 50° for the FA, 930 Hz/pixel for the BW, and 10 mm for the ST. The fixed read-out direction was right to left. An overview of the default settings is provided in Supplementary Table 1. Starting with these default settings, each of the parameters mentioned above was modified, as described in detail in Supplementary Table 2, resulting in acquisition times of 346–1.148 ms per plane. For each parameter modification, the TrueFISP sequence was performed in the same manner. Prior to the start of the fluoroscopic TrueFISP sequence, the correct angles (accepted deviation of 2°) between the needles and the B_0 field and the position in the isocenter of the MR scanner were verified using test sequences.

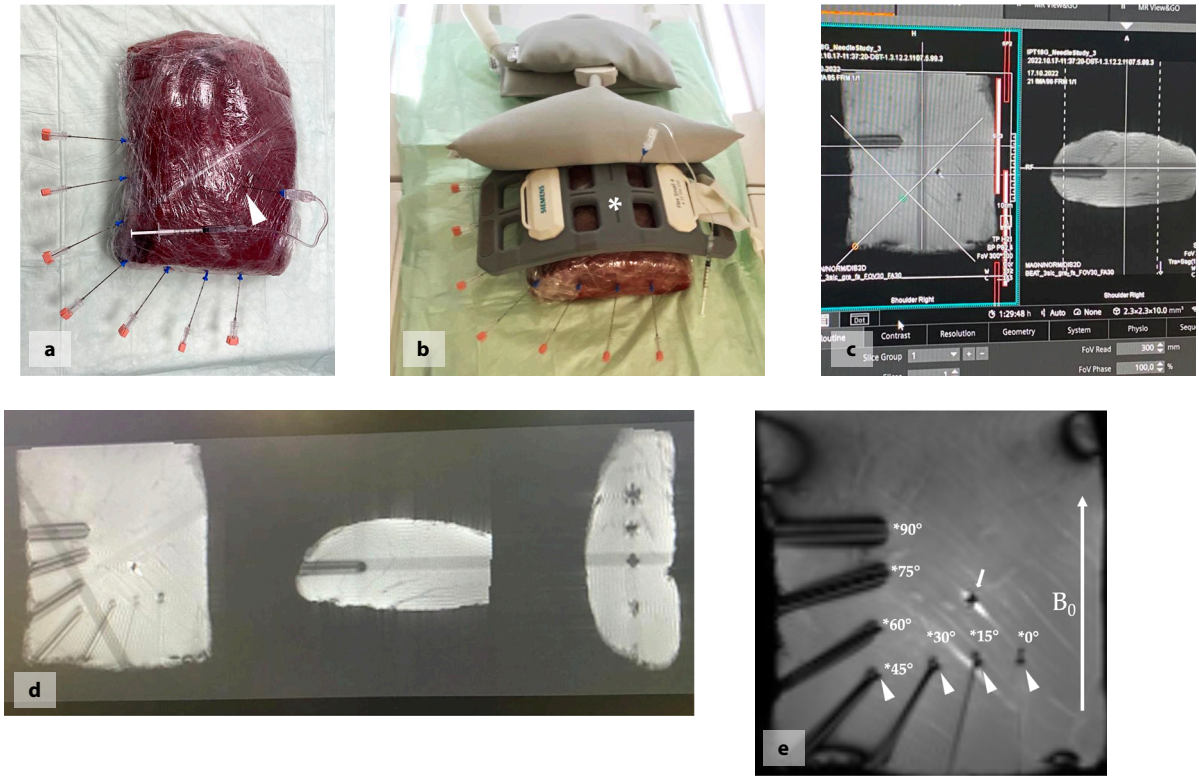

Figure 1. Experimental study set-up. **(a)** Bovine derived muscle phantom model with a 20G Nitinol needle (arrowhead) and linked 1.0-mL syringe for the application of the sodium chloride-diluted-gadolinium centrally into the muscle tissue and seven 18G coaxial Nitinol needles positioned at 0°, 15°, 30°, 45°, 60°, 70°, and 90° relative to the static magnetic field (B_0) field; **(b)** muscle phantom within the 3.0 T magnetic resonance imaging (MRI) scanner covered by a four-channel flex coil (asterisk); **(c)** MRI console illustrating the use of the prototype real-time fluoroscopic MRI software when placing the coaxial needles at defined angles in relation to the B_0 field; **(d)** scan example demonstrating simultaneous acquisition of axial, sagittal, and coronal datasets; **(e)** axial image illustrating the direction of the B_0 field, the simulated contrast-enhanced target lesion at the center of the muscle phantom (small arrow), and the seven coaxial Nitinol needles, which were placed at defined angles relative to the B_0 field (asterisks). Note the ball-like tip artifact at the needle tips at the 0°-, 15°-, 30°-, and 45°-positioned needles (arrowheads). G: gauge; T, tesla.

Artifact diameter measurement

For image acquisition and evaluation of the artifact diameter, Visage Imaging software (Visage Imaging GmbH, Berlin, Germany) was used. The artifact diameters were measured in a standardized plane at two predefined positions (50% and 25% of the inserted needle length measured from the tip of the needle) for every modification of the scan series to ensure comparability. If there was a ball-like tip artifact (IA: 0°, 15°, 30°, and 45°), the maximum diameter of this artifact was determined in the same standardized plane regardless of its two-dimensional direction of largest extension (Figure 2). The needle artifacts were measured by two independent and blinded readers (V.F.S. and S.S.G.) with three and four years of diagnostic MRI experience, respectively, for each modification of the evaluated parameters.

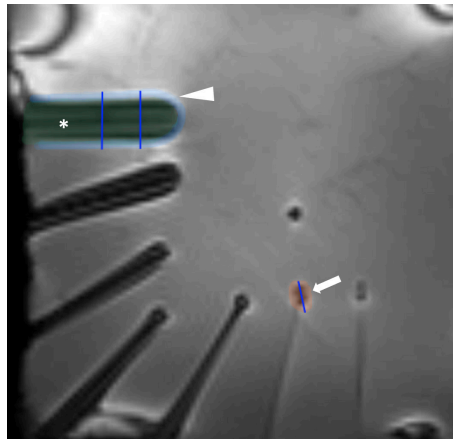

Figure 2. Schematic of the measurement method. The asterisk denotes the hypointense artifact part of the needle artifact at an intervention angle (IA) of 90° (marked in green). The arrowhead presents the additional hyperintense artifact rim around the central hypointense needle artifact occurring at flip angles of 10° and 20° (exemplarily marked in blue for the needle that was inserted at an IA of 90°). The ball-like tip artifact, which occurred at IAs of 0°, 15°, 30°, and 45° is exemplarily shaded orange for the needle that was inserted at an IA of 15°. The three blue lines indicate the measurements of the artifact diameters, first, at two predefined positions (50% and 25% of the inserted needle length measured from the tip of the needle) for every modification of the scan series, and second, as the maximum diameter of the ball-like tip artifact regardless of its two-dimensional direction of largest extension.

Contrast-enhanced target lesion to non-enhanced muscle tissue ratio

For the evaluation of the contrast ratio of the contrast-enhanced target lesion to the non-enhanced muscle tissue, regions of interests (ROIs) with a diameter of at least 5 mm^2 were used to quantitatively assess corresponding signal intensities (SI). The primary ROI was placed inside the contrast-enhanced target lesion and the second ROI within the adjacent non-enhanced muscle tissue at a distance of 20 mm while sparing visible muscle inhomogeneities. In addition,

the latter ROI placement was defined at an identical anatomical depth to the target lesion to avoid any potential influence from surface coil sensitivity profiles. The position, size, and shape of the ROIs were kept almost identical for all measurements. The contrast-enhanced target lesion to non-enhanced muscle tissue contrast ratio (*R*) was defined in terms of the following formula based on the mean SIs in the ROIs:

$$R = SI_{\text{contrast-enhanced target lesion}} / SI_{\text{non-enhanced muscle tissue}}$$

Statistical analysis

Statistical analysis was performed using dedicated statistics software (SPSS version 26, SPSS Inc., Chicago, IL, USA). For the descriptive statistics, the numerical values were presented as means ± standard deviation at 95% confidence intervals. To evaluate the differences between the modified sequence parameters in the related samples, the Wilcoxon signed-rank test (in the case of two values of the modified parameter) and the Friedman test (in the case of more than two values) including post-hoc testing and Bonferroni multiple testing correction were used. Furthermore, possible positive or negative correlations between the values of the modified parameters and the size of the artifact diameter, as well as the contrast-enhanced target lesion to non-enhanced muscle tissue contrast ratio were evaluated. For this purpose, the Bravais–Pearson correlation coefficient was calculated and tested for significance on both sides. To assess the significance of the results, the effect strength, *r*, of the Bravais–Pearson correlation coefficient was additionally presented using Cohen's classification ($r = 0.10$: weak effect, $r = 0.30$: medium effect, $r = 0.50$: strong effect). To determine the differences between the IAs of the MR-compatible needles as unrelated samples, the Kruskal–Wallis test was used. To measure the interrater reliability between the two blinded readers, the intraclass correlation coefficient (ICC) was calculated. A *P* value of 0.05 was set as the limit of statistical significance.

Results

Intervention angle

The seven IAs (0°–90°) exhibited significant differences ($P < 0.001$) in artifact diameters (Figures 3-5), with the artifacts increasing considerably with higher IAs, which also proved to be significant for multiple pairwise comparisons (14 pairs) (Supplementary Table 3). Here, only seven pairwise comparisons of stepwise increased IAs did not show any significant differences (Supplementary Table 3).

Artifact diameters at 50% and 25% of the inserted 18G coaxial Nitinol needle length at various sequence parameters as a function of the intervention angle

The mean values and standard deviations of needle shaft artifact diameters as a function of the IA in relation to the B_0 field of both readers are presented in Table 1.

Flip angle

The artifact size decreased gradually with an increase in FA for each IA (IA_0: 1.40–7.05 mm, IA_{15}: 5.05–7.40 mm, IA_{30}: 7.15–12.35 mm, IA_{45}: 9.85–15.45 mm, IA_{60}: 11.30–16.25 mm, IA_{75}: 14.55–19.45 mm, IA_{90}: 18.90–24.85 mm; $P < 0.001$) (Supplementary Figure 1). The pairwise comparison did not reveal any significant differences among the stepwise increased parameters. However, the multi-

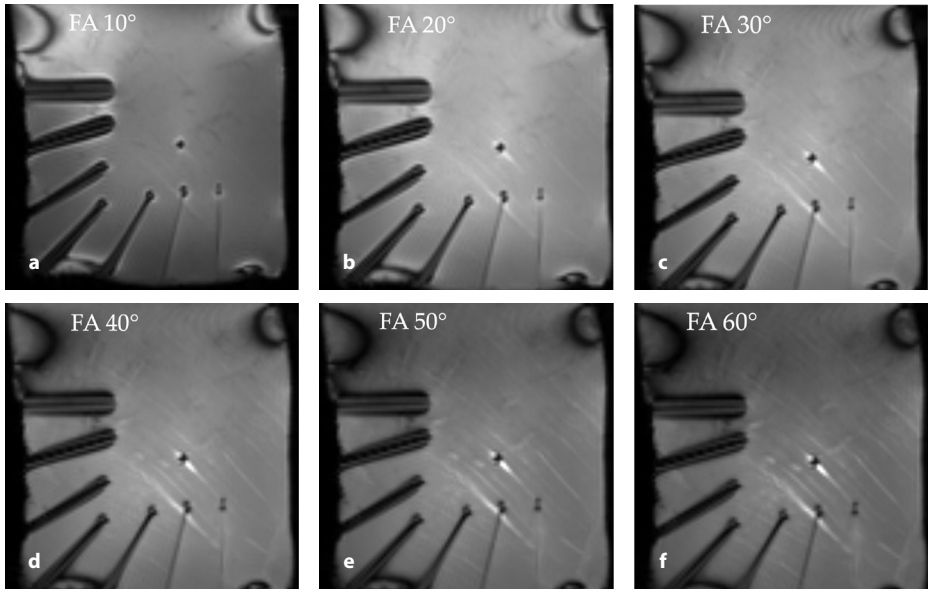

Figure 3. Scan series with flip angles (FA) of 10°–60°. Note the negative correlation of artifact diameters with increasing FAs ($P < 0.001$) **(Supplementary Figure 1)**. **(a-f)** For all seven intervention angles, significant and strong positive correlations between the FAs and the artifact diameters were observed (r = between −0.910 and −0.981; $P < 0.01$). Note the hyperintense peripheral rim around the central hypointense needle artifact occurring at FAs of 10° and 20°.

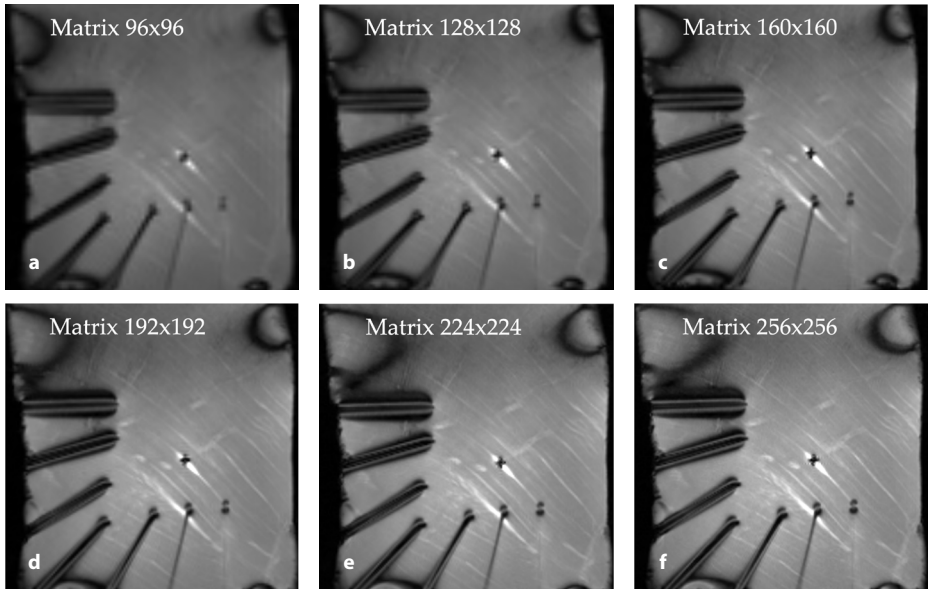

Figure 4. Scan series with matrices of 96 × 96, 128 × 128, 160 × 160, 192 × 192, 224 × 224, and 256 × 256. No significant differences among the artifact diameters were observed when comparing six matrix sizes for all intervention angles (IAs) ($P = 0.035$). However, significant positive correlations were found between the mean artifact diameters of both readers and the matrix size for IAs of 75° and 90° ($r = 0.873$, $P = 0.023$; $r = 0.969$, $P = 0.001$, respectively). In **(a-f)**, the visual correlates are shown. Note an increased differentiation of the actual needle and the needle artifact with larger matrices.

ple testing revealed significant differences among four pairs of FAs (Supplementary Table 4). For all seven IAs, significant and strong positive correlations between the FAs and the artifact diameters were observed (r = –0.973, P = 0.001; r = –0.910, P = 0.012; r = –0.981, P < 0.001; r = –0.970, P = 0.001; r = –0.973, P = 0.001; r = –0.978, P < 0.001; r = –0.919, P = 0.010) (Figure 3). In addition to the central hypointense needle artifact, a hyperintense peripheral rim was observed at FAs of 10° and 20°, which was included in the artifact diameter measurements.

Bandwidth

On modifying the receiver BW, no significant difference in artifact diameter was found for any of the different IAs (IA_0: 3.45–3.90 mm, IA_{15}: 6.15–6.25 mm, IA_{30}: 8.00–8.55 mm, IA_{45}: 11.40–11.75 mm, IA_{60}: 11.90–12.85 mm, IA_{75}: 15.75–15.90 mm, IA_{90}: 18.90–20.25 mm; P = 0.594) and neither was there a sig-

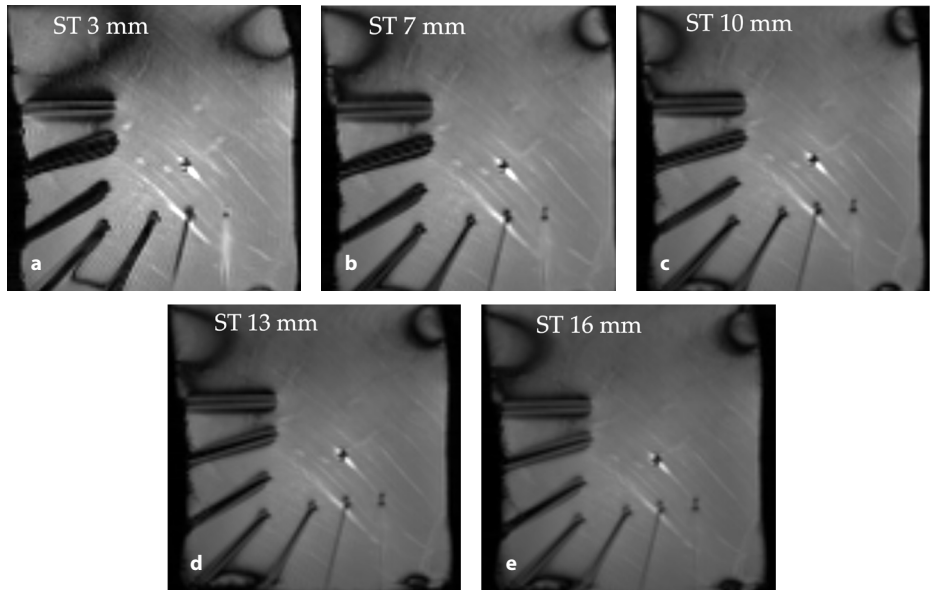

Figure 5. Scan series with slice thicknesses (ST) of 3, 7, 10, 13, and 16 mm. **(a-e)** A significant correlation between the artifact diameters and the ST was found for intervention angles of 45°, 60°, 75°, and 90° (r = –0.943, P = 0.016; r = –0.933, P = 0.020; r = –0.880, P = 0.049, r = –0.955, P = 0.011) **(Supplementary Figure 2)**.

Table 1. Mean artifact diameters measured at 50% and 25% of the inserted needle length

Intervention angle (°)	0	15	30	45	60	75	90	
Parameter								***P* value**
Flip angle (°)								$P < 0.001$[1]
10	7.05 ± 0.07	7.25 ± 0.07	12.35 ± 0.07	15.45 ± 0.07	16.25 ± 0.07	19.45 ± 0.07	24.85 ± 0.07	
20	6.50 ± 0.14	7.40 ± 0.14	10.80 ± 0.14	15.15 ± 0.07	15.45 ± 0.07	17.55 ± 0.07	22.65 ± 0.21	
30	5.70 ± 0.00	7.20 ± 0.00	9.35 ± 0.07	12.65 ± 0.07	13.35 ± 0.07	16.95 ± 0.07	20.25 ± 0.07	
40	2.95 ± 0.07	5.40 ± 0.00	8.60 ± 0.00	12.60 ± 0.00	12.65 ± 0.07	16.30 ± 0.00	19.65 ± 0.07	
50	2.00 ± 0.14	5.35 ± 0.07	8.00 ± 0.00	11.65 ± 0.07	12.30 ± 0.00	14.85 ± 0.07	18.90 ± 0.00	
60	1.40 ± 0.00	5.05 ± 0.07	7.15 ± 0.07	9.85 ± 0.07	11.30 ± 0.00	14.55 ± 0.07	19.10 ± 0.14	
Bandwidth (Hz/pixel)								$P = 0.594$[1]
930	3.90 ± 0.00	6.25 ± 0.00	8.25 ± 0.07	11.75 ± 0.07	11.90 ± 0.00	15.75 ± 0.00	20.25 ± 0.07	
1149	3.45 ± 0.07	6.20 ± 0.00	8.55 ± 0.07	11.65 ± 0.07	12.05 ± 0.07	15.80 ± 0.00	19.95 ± 0.07	
1395	3.55 ± 0.07	6.15 ± 0.07	8.05 ± 0.07	11.45 ± 0.07	12.65 ±0.07	15.85 ± 0.07	18.90 ± 0.00	
1698	3.55 ± 0.07	6.20 ± 0.00	8.00 ± 0.00	11.40 ± 0.00	12.85 ± 0.07	15.90 ± 0.14	19.25 ± 0.07	
Matrix (voxels)								$P = 0.335$[1]
96 × 96	3.90 ± 0.00	6.85 ± 0.07	8.70 ± 0.14	10.35 ± 0.07	13.85 ± 0.07	17.20 ± 0.00	19.70 ± 0.00	
128 × 128	3.95 ± 0.07	6.55 ± 0.07	8.60 ± 0.00	10.30 ± 0.00	13.85 ± 0.07	17.60 ± 0.14	20.75 ± 0.07	
160 × 160	3.95 ± 0.07	5.85 ± 0.07	8.90 ± 0.00	11.95 ± 0.07	14.10 ± 0.00	17.55 ± 0.07	21.45 ± 0.07	
192 × 192	3.95 ± 0.07	5.05 ± 0.07	8.65 ± 0.07	11.65 ± 0.07	13.90 ± 0.14	18.10 ± 0.14	22.10 ± 0.00	
224 × 224	3.25 ± 0.07	6.55 ± 0.00	8.80 ± 0.00	10.90 ± 0.00	12.25 ± 0.07	17.95 ± 0.07	24.75 ± 0.07	
256 × 256	3.25 ± 0.07	4.70 ± 0.00	9.65 ± 0.07	11.05 ± 0.07	13.55 ± 0.07	18.00 ± 0.14	26.40 ± 0.00	
Slice thickness (mm)								$P < 0.001$[1]
3	6.40 ± 0.00	6.80 ± 0.14	9.05 ± 0.07	12.65 ± 0.07	15.65 ± 0.07	19.75 ± 0.07	26.25 ± 0.07	
7	5.05 ± 0.07	6.05 ± 0.07	8.85 ± 0.07	12.15 ± 0.07	13.85 ± 0.07	16.70 ± 0.00	24.60 ± 0.00	
10	5.00 ± 0.00	7.85 ± 0.07	9.25 ± 0.07	11.80 ± 0.00	13.70 ± 0.00	16.40 ± 0.00	22.30 ± 0.14	
13	5.35 ± 0.07	7.70 ± 0.07	8.80 ± 0.00	11.45 ± 0.07	13.50 ± 0.14	16.25 ± 0.07	22.25 ± 0.21	
16	3.20 ± 0.00	4.90 ± 0.14	7.25 ± 0.07	10.10 ± 0.14	11.40 ± 0.00	15.65 ± 0.07	18.10 ± 0.14	
Read-out direction								$P = 0.785$[2]
R >> L	4.30 ± 0.00	6.45 ± 0.07	8.20 ± 0.14	10.70 ± 0.00	13.40 ± 0.14	17.35 ± 0.07	20.80 ± 0.14	
A >> P	4.30 ± 0.00	6.45 ± 0.07	8.35 ± 0.07	10.95 ± 0.00	13.35 ± 0.14	17.20 ± 0.00	20.75 ± 0.07	

Artifact diameters averaged over both readers at 50% and 25% of the needle length measured from the tip of the needle (in mm) at various sequence parameters as a function of the intervention angle in relation to the B_0 field. Values are presented as means ± standard deviation. [1]Friedman test; [2]Wilcoxon signed-rank test; R, right; L, left; A, anterior; P, posterior.

nificant correlation between the artifact diameter and the BW (r = –0.576, P = 0.424; r = –0.575, P = 0.425; r = –0.680, P = 0.320; r = 0.746, P = 0.254; r = 0.573, P = 0.427; r = –0.817, P = 0.188).

Matrix

The Friedman test revealed no significant differences between the artifact diameters when comparing six matrix sizes for each IA (IA_0: 3.25–3.95 mm, IA_{15}: 4.70–6.85 mm, IA_{30}: 8.60–9.65 mm, IA_{45}: 10.30–11.95 mm, IA_{60}: 12.25–14.10 mm, IA_{75}: 17.20–18.10 mm, IA_{90}: 19.70–26.40 mm; P = 0.335). In addition, the pairwise comparisons did not indicate any significant differences (P = 1.000) (Supplementary Table 4). However, significant positive correlations were found between the mean artifact diameters of both readers and the matrix for the IAs of 75° and 90° (r = 0.873, P = 0.023; r = 0.969, P = 0.001, respectively) (Figure 4). For the other IAs, there was no significant correlation between the artifact diameter and the matrix. In addition, an increased differentiation between the display of the actual needle and the surrounding needle artifact was observed with larger matrices.

Slice thickness

On modifying the ST, significant differences in artifact diameter were found for each IA (IA_0: 3.20–6.40 mm, IA_{15}: 4.90–7.85 mm, IA_{30}: 7.25–9.25 mm, IA_{45}: 10.10–12.65 mm, IA_{60}: 11.40–15.65 mm, IA_{75}: 15.65–19.75 mm, IA_{90}: 18.10–26.25 mm; P < 0.001) (Supplementary Figure 2). The multiple testing revealed significant differences between the STs of 3 and 17 mm (P < 0.001) (Supplementary Table 4). A significant correlation between the artifact diameters and ST was found for IAs of 45°, 60°, 75°, and 90° (r = –0.943, P = 0.016; r = –0.933, P = 0.020; r = –0.880, P = 0.049, r = –0.955, P = 0.011) (Figure 5).

Read-out direction

For the two different read-out directions (right >> left, anterior >> posterior), no significant differences in artifact diameters were found during the Wilcoxon signed-rank test (P = 0.785), with generally similar artifact diameters for both read-out directions.

Artifact diameters at the tip of the 18G coaxial Nitinol needle at various sequence parameters as a function of the intervention angle

The mean values and standard deviations of the artifact diameters at the needle tip as a function of the IA in relation to the B_0 field of

Table 2. Mean maximum ball-like tip artifact diameters (regardless of its two-dimensional direction of largest extension)

Intervention angle (°)	0	15	30	45	
Parameter					***P* value**
Flip angle (°)					$P = 0.003$[1]
10	13.10 ± 0.00	13.10 ± 0.00	12.10 ± 0.00	12.25 ± 0.07	
20	11.85 ± 0.07	12.05 ± 0.07	12.75 ± 0.07	11.50 ± 0.00	
30	10.25 ± 0.07	10.50 ± 0.14	9.95 ± 0.07	10.95 ± 0.07	
40	10.25 ± 0.07	9.35 ± 0.07	9.45 ± 0.07	9.65 ± 0.07	
50	10.05 ± 0.07	9.45 ± 0.07	9.30 ± 0.00	8.50 ± 0.14	
60	9.50 ± 0.07	9.10 ± 0.00	9.20 ± 0.00	9.15 ± 0.14	
Bandwidth (Hz/pixel)					$P = 0.082$[1]
930	11.10 ± 0.00	10.80 ± 0.14	10.15 ± 0.07	10.15 ± 0.07	
1149	11.85 ± 0.07	10.40 ± 0.00	9.95 ± 0.07	9.95 ± 0.07	
1395	11.50 ± 0.14	10.15 ± 0.07	10.60 ± 0.14	9.70 ± 0.00	
1698	11.90 ± 0.14	10.80 ± 0.00	10.75 ± 0.07	10.30 ± 0.00	
Matrix (voxels)					$P = 0.614$[1]
96 × 96	13.10 ± 0.00	10.55 ± 0.05	10.30 ± 0.00	10.05 ± 0.05	
128 × 128	12.00 ± 0.10	11.15 ± 0.05	10.60 ± 0.10	10.85 ± 0.05	
160 × 160	11.80 ± 0.00	10.05 ± 0.05	10.35 ± 0.05	10.30 ± 0.00	
192 × 192	10.70 ± 0.10	10.65 ± 0.05	10.75 ± 0.05	9.80 ± 0.10	
224 × 224	12.20 ± 0.00	11.50 ± 0.00	11.20 ± 0.05	9.05 ± 0.05	
256 × 256	11.75 ± 0.05	11.95 ± 0.05	10.15 ± 0.05	10.30 ± 0.00	
Slice thickness (mm)					$P = 0.163$[1]
3	10.30 ± 0.00	11.65 ± 0.05	10.80 ± 0.00	10.65 ± 0.05	
7	10.25 ± 0.05	10.15 ± 0.05	9.90 ± 0.10	9.50 ± 0.10	
10	10.90 ± 0.10	11.05 ± 0.05	10.45 ± 0.05	10.30 ± 0.10	
13	11.05 ± 0.05	10.80 ± 0.10	10.15 ± 0.05	10.30 ± 0.00	
16	11.80 ± 0.00	11.25 ± 0.05	8.45 ± 0.05	8.65 ± 0.05	
Read-out direction					$P = 0.465$[2]
RL	11.00 ± 0.00	10.05 ± 0.05	9.45 ± 0.05	9.65 ± 0.05	
AP	11.20 ± 0.00	10.80 ± 0.10	9.70 ± 0.10	9.30 ± 0.00	

The tip artifact diameters averaged over both readers at various sequence parameters as a function of the intervention angle in relation to the B_0 field. The values are presented as means ± standard deviation; [1]Friedman test; [2]Wilcoxon signed-rank test; R, right; L, left; A, anterior; P, posterior.

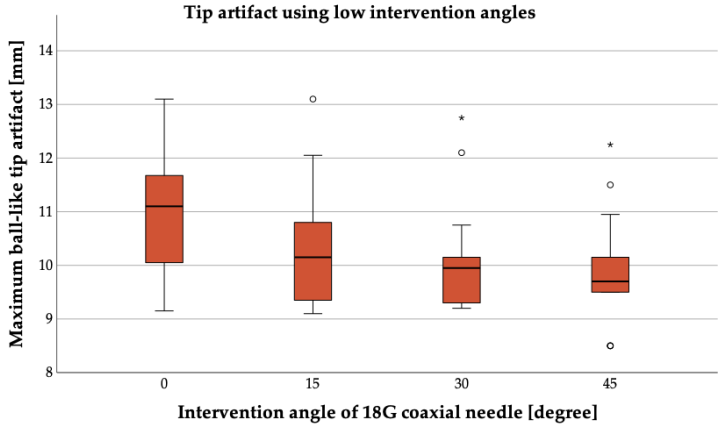

Figure 6. Behavior of the ball-like tip artifact, which occurred at intervention angles (IAs) of 0°, 15°, 30°, and 45°. The maximum diameter of this artifact increased gradually with a decrease in IA (P = 0.022). The pairwise comparisons revealed significant differences between 0° and 30° (P = 0.041), as well as between 0° and 45° (P = 0.047).

Table 3. Interrater reliability

Intervention angle (°)	ICC value	*P* value	95% confidence interval
0	0.998	<0.001	0.995 – 0.999
15	0.994	<0.001	0.985 – 0.997
30	0.995	<0.001	0.989 – 0.998
45	0.999	<0.001	0.997 – 0.999
60	0.997	<0.001	0.994 – 0.999
75	0.998	<0.001	0.995 – 0.999
90	0.998	<0.001	0.996 – 0.999

The ICC values of two blinded readers are shown for intervention angles of 0°–90°. ICC, intraclass correlation coefficient.

both readers are presented in Table 2. A ball-like tip artifact occurred using low IAs of 0°–45°. The maximum diameter of this artifact increased gradually with a decrease in IA ($P = 0.022$) (Figure 6). The pairwise comparisons revealed significant differences between 0° and 30° ($P = 0.041$), as well as between 0° and 45° ($P = 0.047$) (Supplementary Table 5). The modification of the sequence parameters, BW, matrix, ST, read-out direction, had no significant influence on this artifact ($P = 0.082$, $P = 0.614$, $P = 0.163$, $P = 0.465$), while that of the FA did ($P = 0.003$).

Interrater reliability

For the various IAs (0° 15°, 30°, 45°, 60°, 75°, 90°), the ICCs were 0.998, 0.994, 0.995, 0.999, 0.997, 0.998, and 0.998, respectively ($P < 0.001$), indicating excellent interrater reliability (Table 3).

Contrast-enhanced target lesion to non-enhanced muscle tissue contrast ratio

The lesion-to-muscle-contrast ratio, *R*, presented significant positive correlations with an increase in FA and matrices ($P < 0.001$; $P = 0.003$), as well as a significant negative correlation with an increase in ST ($P = 0.007$). No significant correlations were found for the modified BWs ($P = 0.171$). The corresponding data are presented as supplemental information (Supplementary Table 6).

Discussion

In this 3.0 T musculoskeletal phantom study, the influence of different sequence parameters of an interventional real-time fluoroscopic pulse sequence with TrueFISP contrast on the artifact behavior of a commercially available MR-compatible coaxial 18G Nitinol needle was investigated as a function of the IA.

Needle artifacts pose a major limitation to high-field MRI-guided interventions in particular, regardless of the intended target, and are caused by several different physical processes, of which inhomogeneities of the B_0 field experienced by the nuclei are the most important. This needle-induced B_0 inhomogeneity is caused by the geometric characteristics and the individual magnetic susceptibility of the imaged object. Distortions of the spatial geometry, as well as intra-voxel dephasing are caused by these static field errors.[17,23] Among other artifacts, needle artifacts can be caused by radiofrequency effects such as B_1 enhancement.[24] With this background, the present study aimed to analyze artifact formation with a focus on its relevance for MRI-guided high-field musculoskeletal interventional procedures through modifying different sequence parameters (FA, BW, matrix, ST, and read-out-direction) as a function of the IA. Completely erased or too-small artifacts are not always desirable in MR-guided intervention since the needle is visualized by the artifact itself and minimizing artifacts can mean the needle is difficult to recognize.

In general, the technological advances in magnet, coil, protocol, biopsy needle, and probe design have made MRI-guidance a clinically valuable imaging technique for minimally invasive procedures. Due to the continuing innovations in augmented reality, targeting software, and compatible devices, it is crucial to reassess methodological and technical fundamentals, such as needle artifacts. This is especially the case for MRI-guided procedures for musculoskeletal interventions, which is an extremely new field, and specific adaptations need to be made. As such, a phantom that has been adapted to the target tissue in musculoskeletal interventions (muscle phantom) was selected, in contrast to previous studies, which generally employed a 3 T MRI scanner.[25,26] Singh et al.[25] evaluated needle artifact diameters using an acrylic phantom modifying only two parameters: IA and read-out direction. Furthermore, in the present study, contrast medium application was also performed for experimental evaluation of the visibility of the target lesion and to emulate as far as possible the clinical routine, exemplarily imitating contrast-enhanced MR-guided punctures of joint structures in the case of capsulitis.

It is well known that the IA is closely associated with the artifact size.[17,22,27] In line with this, the seven IAs (0°–90°) analyzed in this study exhibited significant differences in artifact diameters, with the artifacts increasing considerably with higher IAs, which also proved to be significant for most of the multiple pairwise comparisons. Elsewhere, Schmidt et al.[20] demonstrated a positive correlation between artifact size and increasing IAs in their 1.5 T-liver phantom study. At this point, it should be noted that it is advantageous to use low susceptibility materials since these can be used at higher IAs. In addition, Frahm et al.[28] analyzed the relationship between the magnetic field strength and the IA. The authors found that the needle artifact growth with an increase in IA was lower with a 0.2-T field strength than with a 1.5-T strength and that at high-field strengths, the artifact size correlated closely with an increase in IA relative to the B_0 field.[28]

In the present study, decreasing artifact diameters were observed with an increase in FA for each IA. At FAs of 10° and 20°, an additional hyperintense peripheral rim artifact was observed around the otherwise hypointense artifact along the shaft of the needle, which was included in the measurements. This artifact consecutively extends the area of potential misinterpretation of the actual needle position and needs to be considered when choosing a FA of 10° or 20° for the TrueFISP sequence. Interestingly, in a previous liver phantom study by Schmidt et al.[20] that analyzed a T1-weighted gradient echo (GRE) sequence at 1.5 T, this hyperintense peripheral rim artifact was observed at high FAs of >45°. Another previous investigation of needle artifacts by Bauch[29], who also modified the FA in a T1-weighted GRE sequence, revealed no relevant changes to the artifact diameter in a stepwise comparison for FAs of <45°, which is in line with both the results of the present study and those obtained by Schmidt et al.[20] However, a T1-weighted GRE sequence was analyzed in these studies and therefore these results cannot be expected to be directly transferrable to ours. This notwithstanding, the multiple testing revealed significant differences between four pairs of FAs, and significant and strong positive correlations between FA and artifact diameter were observed in the present study for all seven IAs. While the previous investigations

demonstrated optimal artifact behavior with FAs of <45° for T1-weighted GRE sequences,[20,29] in contrast, the present study found the smallest artifact sizes with higher FAs (>40°).

No significant correlation was found between artifact diameter and modifications of the BW, although varying the BW is reported in the literature to be a crucial parameter for the minimization of needle artifacts.[30] The physical context is that the Larmor frequencies of the hydrogen protons are altered to a certain amount by a metallic object of a given size and susceptibility. Thus, reducing the BW increases the number of pixels that are visibly affected by the variance in frequencies and consecutively increases the size of the susceptibility artifact.[31] However, this finding using a TrueFISP sequence is consistent with Schmidt et al.'s[20] results when analyzing the BW as a potential influencing parameter on artifact diameters for a T1-weighted GRE sequence, who also did not find any significant differences between different BWs and artifact behavior in a liver phantom. The fact that the BW variations did not significantly influence the needle artifact size may have been because the artifact was too small, meaning potentially significant differences could have remained hidden. However, the BW range in the present study was chosen according to the standard BWs used in clinical practice.

No significant differences in artifact diameter were found when comparing various matrix sizes for each IA, which was also the case with the pairwise comparisons. However, significant positive correlations were found between artifact diameter and matrix for IAs of 75° and 90°. In addition, an increased differentiation between the display of the actual needle and the surrounding needle artifact with larger matrices was observed, which is also in line with Schmidt et al.'s[20] results, who observed smaller artifact diameters at higher matrix sizes in their liver phantom study (not statistically significant). Generally, a higher matrix size reduces the artifact diameters and optimizes the image quality due to decreased voxel volume. In determining the spatial resolution, the matrix is a quality feature of the acquired image data,[28] meaning higher matrices may improve the differentiation of the actual intervention needle and therefore allow for more exact lesion targeting. Nonetheless, the increase in acquisition time is the major reason why matrix sizes cannot be set as high as possible in clinical practice.[29]

The voxel size is not only determined by the matrix, but also by the ST. A decrease in ST is equivalent to a reduction in voxel size and leads to a decreased field inhomogeneity within each individual voxel and subsequently results in lower artifact dependence and the generation of smaller needle artifacts.[28,32] In the present study, significant differences in artifact diameters were observed for each IA when modifying the ST. In addition, the multiple testing revealed significant differences between STs of 3 and 16 mm, and a significant correlation between the artifact diameters and the ST was found for IAs of 45°, 60°, 75°, and 90°. However, in our study setting, smaller artifact sizes were found for higher STs. In this context, it must be noted that the artifact size in the ST-modified scan series appears to be highly influenced by different IAs and that the differentiation of the actual needle shaft and tip is much better with higher STs (>10 mm) when looking at higher IAs. However, it should also be remembered that the ST should not be set too high during the procedure to allow for accurate needle placement. Thus, a potential compromise is selecting a ST of >7 mm. No significant differences in needle artifact sizes were observed for the two different read-out directions (RL or AP) in this study. This is consistent with previous studies on T1-weighted GRE sequences,[18,20,28] but not with a previous study on spin-echo and turbo spin-echo sequences, in which the artifacts were more pronounced when the read-out direction was perpendicular to the needle shafts.[18]

Ball-like tip artifacts were observed with low IAs of 0°–45° and these increased in size with a decrease in IA. Interestingly, this artifact was not significantly influenced by any sequence parameter other than the FA. This artifact at the needle tip particularly impairs the visibility of the tip, which makes precise needle guidance difficult and can be expected to affect the targeting accuracy. Moreover, it is problematic that this tip artifact extends in all directions such that it often resembles a ball; hence the "ball-like" description.[29,33] In line with our results, this tip artifact occurred with low IAs of 0°–10° in a previous study by Schmidt et al.[20] As previously described by Liu et al.[34], the B_0 field is most strongly influenced in the area around the needle tip, which is particularly noticeable in materials with lower magnetic susceptibility, such as carbon fiber or titanium, when compared with other materials (e.g., chromium, cobalt, or nickel).

Regarding clinical routine high-field musculoskeletal interventional procedures, we recommend using a FA of 40°–60° to minimize hypointense artifact formation around the needle shaft and to avoid the occurrence of additional hyperintense artifact formation, which only occurred at low FAs of 10° and 20° in the present scan series. In addition, an ST of 10–16 mm returned the best image quality. To specifically avoid ball-like tip artifacts, IAs of 45°–60° should be selected.

Furthermore, it is important to not only minimize needle artifacts but also to guarantee sufficient visibility of the target lesion. Therefore, the contrast ratio of a gadolinium-enhanced target lesion placed centrally into the muscle phantom and that of the adjacent non-enhanced muscle tissue were evaluated by quantitatively analyzing the corresponding SIs. The contrast-enhanced target lesion was best visualized at higher FAs (40°–60°) and matrices (224 × 224/256 × 256), while a negative correlation between the visibility of the target lesion with increasing STs was observed, which can be explained by the increasing partial-volume effects at higher STs. For small lesions (relative to the ST), this might lead to a potential conflict since higher STs of 10–16 mm minimized the needle artifacts while maintaining the best possible visualization of the coaxial intervention needle. To the best of the authors' best knowledge, there are no comparable previous studies that investigated the visibility of a contrast-enhanced lesion in a similar setting.

However, this study involves a number of potential limitations. First, a fixed phantom was used, which provided an optimal background signal intensity and therefore an optimized depiction of signal voids. In an *in vivo* setting, it must be assumed that both the image quality and the artifact contrast will be worse due to, for example, motion artifacts. Second, this phantom study was performed at a single field strength (3.0 T), and lower field strengths (e.g., 1.5 T) will need to be investigated with this TrueFISP sequence in view of scenarios such as when the patient is not suitable for a high-field intervention due to only 1.5 T-conditional external materials. Nevertheless, 3.0 T is the preferable field strength in the majority of musculoskeletal investigations. Third, only a single alloy (Nitinol) and a single needle size (18G) were investigated. As both alloy and needle size have an impact on artifact behavior,[29,33] further studies are needed to examine these effects. Fourth, the artifact diameters were determined by manual measurements and automatized artifact measurements would minimize any potential reader bias. However, high inter-reader agreement was observed in our study. Furthermore, the artifact di-

ameters were measured in two-dimensional terms and it must be acknowledged that needle artifacts occur three-dimensionally and that the needle artifact volume might be a relevant parameter for exact needle guidance. Nonetheless, depending on the sequence acquisitions, it might not be adequately feasible to conduct such measurements with the available fluoroscopic MRI hardware and software. Fifth, only one single sequence parameter was modified in our scan series to avoid any additional confounding variable; however, the BW was not modified separately but only coupled to the TR since the minimum TR had been systematically chosen in our experimental setting. Furthermore, while the image quality will not be affected by increasing motion artifacts with longer scan times (with an increase in TR) in a phantom model, it may be in real-world settings. Sixth, minimized artifact diameters do not necessarily imply that the "true" position of the needle within the tissue is better known, as it is inherently difficult to be certain about the exact needle position from real-time fluoroscopic MRI visualization. Therefore, further studies with coordinate registration are needed to ensure more accurate verification of the exact needle position and, in particular, the position of the needle tip. In a previous study, Yamada et al.[35] applied real-time ultrasound imaging fused with reformatted static MR images and coordinate registration for needle guidance during MR-guided percutaneous tumor ablations and revealed targeting errors of 1.6 ± 0.6 mm. Last, the investigated sequence parameter settings need to be analyzed and adapted to clinical use cases.

In conclusion, to minimize needle artifacts, it is recommended to use FAs of 40°–60°, a ST of >7 mm, and, if possible, an IA of 45°–60°. The visibility of the target lesion and the needle's artifact behavior must be weighed up against each other when choosing the ST, while higher FAs (40°–60°) and matrices (224 × 224/256 × 256) are associated with low artifacts and sufficient lesion visibility.

Acknowledgements

We would like to thank Siemens Healthineers (Erlangen, Germany) for their support in the development of this manuscript and for providing the real-time sequences and associated software ("Needle Intervention Add-in" package).

Conflict of interest disclosure

The authors declared no conflicts of interest.

References

1. Barkhausen J, Kahn T, Krombach GA, et al. White paper: interventional MRI: current status and potential for development considering economic perspectives, part 1: general application. *Rofo*. 2017;189(7):611-623. [CrossRef]
2. Bock M, Umathum R, Zuehlsdorff S, et al. Interventional magnetic resonance imaging: an alternative to image guidance with ionising radiation. *Radiat Prot Dosimetry*. 2005;117(1-3):774-778. [CrossRef]
3. Elfatairy KK, Filson CP, Sanda MG, Osunkoya AO, Nour SG. In-Bore MRI-guided prostate biopsies in patients with prior positive transrectal US-guided biopsy results: pathologic outcomes and predictors of missed cancers. *Radiol Imaging Cancer*. 2020;2(5):e190078. [CrossRef]
4. Fischbach F, Thormann M, Seidensticker M, Kropf S, Pech M, Ricke J. Assessment of fast dynamic imaging and the use of Gd-EOB-DTPA for MR-guided liver interventions. *J Magn Reson Imaging*. 2011;34(4):874-879. [CrossRef]
5. Jungmann PM, Agten CA, Pfirrmann CW, Sutter R. Advances in MRI around metal. *J Magn Reson Imaging*. 2017;46(4):972-991. [CrossRef]
6. Weiss J, Hoffmann R, Rempp H, et al. Feasibility, efficacy, and safety of percutaneous MR-guided ablation of small (≤12 mm) hepatic malignancies. *J Magn Reson Imaging*. 2019;49(2):374-381. [CrossRef]
7. Winkelmann MT, Archid R, Gohla G, et al. MRI-guided percutaneous thermoablation in combination with hepatic resection as parenchyma-sparing approach in patients with primary and secondary hepatic malignancies: single center long-term experience. *Cancer Imaging*. 2020;20(1):37. [CrossRef]
8. Winkelmann MT, Gohla G, Kubler J, et al. MR-guided high-power microwave ablation in hepatic malignancies: initial results in clinical routine. *Cardiovasc Intervent Radiol*. 2020;43(11):1631-1638. [CrossRef]
9. Dianat SS, Carter HB, Macura KJ. Magnetic resonance-guided prostate biopsy. *Magn Reson Imaging Clin N Am*. 2015;23(4):621-631. [CrossRef]
10. Fischbach F, Bunke J, Thormann M, et al. MR-guided freehand biopsy of liver lesions with fast continuous imaging using a 1.0-T open MRI scanner: experience in 50 patients. *Cardiovasc Intervent Radiol*. 20211;34(1):188-192. [CrossRef]
11. Fischbach F, Eggemann H, Bunke J, Wonneberger U, Ricke J, Strach K. MR-guided freehand biopsy of breast lesions in a 1.0-T open MR imager with a near-real-time interactive platform: preliminary experience. *Radiology*. 2012;265(2):359-370. [CrossRef]
12. Fritz J, Thomas C, Clasen S, Claussen CD, Lewin JS, Pereira PL. Freehand real-time MRI-guided lumbar spinal injection procedures at 1.5 T: feasibility, accuracy, and safety. *AJR Am J Roentgenol*. 2009;192(4):161-167. [CrossRef]
13. Tempany C, Straus S, Hata N, Haker S. MR-guided prostate interventions. *J Magn Reson Imaging*. 2008;27(2):356-367. [CrossRef]
14. Weiss CR, Nour SG, Lewin JS. MR-guided biopsy: a review of current techniques and applications. *J Magn Reson Imaging*. 2008;27(2):311-325. [CrossRef]
15. Bayer T, Adler W, Janka R, Uder M, Roemer F. Magnetic resonance cinematography of the fingers: a 3.0 tesla feasibility study with comparison of incremental and continuous dynamic protocols. *Skeletal Radiol*. 2017;46(12):1721-1728. [CrossRef]
16. Penzkofer T, Peykan N, Schmidt K, Krombach G, Kuhl CK. How MRI compatible is "MRI compatible"? A systematic comparison of artifacts caused by biopsy needles at 3.0 and 1.5 T. *Cardiovasc Intervent Radiol*. 2013;36(6):1646-1657. [CrossRef]
17. Ladd ME, Erhart P, Debatin JF, Romanowski BJ, Boesiger P, McKinnon GC. Biopsy needle susceptibility artifacts. *Magn Reson Med*. 1996;36(4):646-651. [CrossRef]
18. Lewin JS, Duerk JL, Jain VR, Petersilge CA, Chao CP, Haaga JR. Needle localization in MR-guided biopsy and aspiration: effects of field strength, sequence design, and magnetic field orientation. *AJR Am J Roentgenol*. 1996;166(6):1337-1345. [CrossRef]
19. Lüdeke KM, Röschmann P, Tischler R. Susceptibility artefacts in NMR imaging. *Magn Reson Imaging*. 1985;3(4):329-343. [CrossRef]
20. Schmidt VF, Arnone F, Dietrich O, et al. Artifact reduction of coaxial needles in magnetic resonance imaging-guided abdominal interventions at 1.5 T: a phantom study. *Sci Rep*. 2021;11(1):22963. [CrossRef]
21. Thomas C, Springer F, Röthke M, et al. In vitro assessment of needle artifacts with an interactive three-dimensional MR fluoroscopy system. *J Vasc Interv Radiol*. 2010;21(3):375-380. [CrossRef]
22. Thomas C, Wojtczyk H, Rempp H, et al. Carbon fibre and nitinol needles for MRI-guided interventions: first in vitro and in vivo application. *Eur J Radiol*. 2011;79(3):353-358. [CrossRef]
23. Bakker CJ, Bhagwandien R, Moerland MA, Fuderer M. Susceptibility artifacts in 2DFT spin-echo and gradient-echo imaging: the cylinder model revisited. *Magn Reson Imaging*. 1993;11(4):539-548. [CrossRef]
24. Graf H, Lauer UA, Berger A, Schick F. RF artifacts caused by metallic implants or instruments which get more prominent at 3 T: an in vitro study. *Magn Reson Imaging*. 2005;23(3):493-499. [CrossRef]
25. Singh S, Torrealdea F, Bandula S. MR Imaging-Guided Intervention: Evaluation of MR conditional biopsy and ablation needle tip artifacts at 3T using a balanced fast field echo sequence. *J Vasc Interv Radiol*. 2021;32(7):1068-1074. [CrossRef]

26. DiMaio SP, Kacher DF, Ellis RE, et al. Needle artifact localization in 3T MR images. *Stud Health Technol Inform*. 2006;119:120-125. [CrossRef]
27. Wachowicz K, Thomas SD, Fallone BG. Characterization of the susceptibility artifact around a prostate brachytherapy seed in MRI. *Med Phys*. 2006;33(12):4459-4467. [CrossRef]
28. Frahm C, Gehl HB, Melchert UH, Weiss HD. Visualization of magnetic resonance-compatible needles at 1.5 and 0.2 tesla. *Cardiovasc Intervent Radiol*. 1996;19(5):335-340. [CrossRef]
29. Bauch S. Evaluation MR kompatibler Nadeln und interaktiver Sequenzen zur interventionellen Bildgebung an einem offenen 1.0 tesla MR-tomographen (panorama-HFO). Germany: Otto-von-Guericke University Magdeburg; 2013. [CrossRef]
30. Hargreaves BA, Worters PW, Pauly KB, Pauly JM, Koch KM, Gold GE. Metal-induced artifacts in MRI. *AJR Am J Roentgenol*. 2011;197(3):547-555. [CrossRef]
31. Talbot BS, Weinberg EP. MR Imaging with metal-suppression sequences for evaluation of total joint arthroplasty. *Radiographics*. 2016;36(1):209-225. [CrossRef]
32. Müller-Bierl B, Graf H, Lauer U, Steidle G, Schick F. Numerical modeling of needle tip artifacts in MR gradient echo imaging. *Med Phys*. 2004;31(3):579-587. [CrossRef]
33. Reichenbach JR, Wurdinger S, Pfleiderer SO, Kaiser WA. Comparison of artifacts produced from carbon fiber and titanium alloy needles at 1.5 T MR imaging. *J Magn Reson Imaging*. 2000;11(1):69-74. [CrossRef]
34. Liu H, Hall WA, Martin AJ, Truwit CL. Biopsy needle tip artifact in MR-guided neurosurgery. *J Magn Reson Imaging*. 2001;13(1):16-22. [CrossRef]
35. Yamada A, Tokuda J, Naka S, Murakami K, Tani T, Morikawa S. Magnetic resonance and ultrasound image-guided navigation system using a needle manipulator. *Med Phys*. 2020;47:850-858. [CrossRef]

Supplementary Table 1. Default settings

Fixed parameter	Value
FOV (mm^2)	300 × 300
Matrix (voxels)	128 × 128
Slice thickness (mm)	10
Flip angle (°)	50
Echo time (ms)	1.71
Repetition time (ms)	3.42
Bandwidth (Hz/pixel)	930
Read-out direction	RL
Phase oversampling	0
Acquisition time (ms)	461

While one parameter was modified, all others remained unchanged in a predefined setting. FOV, field of view; R, right; L, left.

Supplementary Table 2. MRI acquisition parameters and values.

	Values	Setting	Coupled TR (ms)
Scan series	1	10	
	2	20	
Flip angle (°)	3	30	
	4	40	
	5	50	
	6	60	
Bandwidth (Hz/pixel)	1	930	3.42
	2	1.149	3.28
	3	1.395	3.20
	4	1.698	3.18
Matrix (voxels)	1	96 × 96	
	2	128 × 128	
	3	160 × 160	
	4	192 × 192	
	5	224 × 224	
	6	256 × 256	
Slice thickness (mm)	1	3	
	2	7	
	3	10	
	4	13	
	5	16	
Read-out direction	1	RL	
	2	AP	

Scan series of study profile for intervention angles relative to the B_0 field of 0°–90°. Systematic and sequential modification of the technical parameters of the TrueFISP sequence. TR, repetition time; Hz, Hertz; R, right; L, left; A, anterior; P, posterior; TrueFISP, true fast imaging with steady-state free precession; MRI, magnetic resonance imaging.

Supplementary Table 3. Pairwise comparisons of the artifact diameter depending on the intervention angle

	Sample 1	Sample 2	
Parameter			***P* value**[1]
Intervention angle (°)			
	0	15	*P* = 1.000
	0	30	***P* = 0.027**
	0	45	***P* = 0.000**
	0	60	***P* = 0.000**
	0	75	***P* = 0.000**
	0	90	***P* = 0.000**
	15	30	*P* = 1.000
	15	45	***P* = 0.004**
	15	60	***P* = 0.000**
	15	75	***P* = 0.000**
	15	90	***P* = 0.000**
	30	45	*P* = 1.000
	30	60	*P* = 0.050
	30	75	***P* = 0.000**
	30	90	***P* = 0.000**
	45	60	*P* = 1.000
	45	75	***P* = 0.036**
	45	90	***P* = 0.000**
	60	75	*P* = 1.000
	60	90	***P* = 0.008**
	75	90	*P* = 1.000

[1]Kruskal–Wallis test, *P* values of post-hoc testing including Bonferroni multiple testing correction.

Supplementary Table 4. Pairwise comparisons of the artifact diameter depending on the modified sequence parameters flip angle, bandwidth, matrix size, and slice thickness

	Sample 1	Sample 2	
Parameter			***P* value**[1]
Flip angle (°)			
	60	50	*P* = 1.000
	60	40	*P* = 0.949
	60	30	*P* = 0.064
	60	20	***P* = 0.001**
	60	10	***P* = 0.000**
	50	40	*P* = 1.000
	50	30	*P* = 0.482
	50	20	***P* = 0.015**
	50	10	***P* = 0.001**
	40	30	*P* = 1.000
	40	20	*P* = 0.482
	40	10	*P* = 0.064
	30	20	*P* = 1.000
	30	10	*P* = 0.949
	20	10	*P* = 1.000
Bandwidth (Hz/pixel)			
	1.395	1.698	*P* = 1.000
	1.395	1.149	*P* = 1.000
	1.395	930	*P* = 1.000
	1.698	1.149	*P* = 1.000
	1.698	930	*P* = 1.000
	1.149	930	*P* = 1.000
Matrix (voxels)			
	96 × 96	224 × 224	*P* = 1.000
	96 × 96	128 × 128	*P* = 1.000
	96 × 96	256 × 256	*P* = 1.000
	96 × 96	192 × 192	*P* = 1.000
	96 × 96	160 × 160	*P* = 1.000
	224 × 224	128 × 128	*P* = 1.000
	224 × 224	256 × 256	*P* = 1.000
	224 × 224	192 × 192	*P* = 1.000
	224 × 224	160 × 160	*P* = 1.000
	128 × 128	256 × 256	*P* = 1.000
	128 × 128	192 × 192	*P* = 1.000
	128 × 128	160 × 160	*P* = 1.000
	256 × 256	192 × 192	*P* = 1.000
	256 × 256	160 × 160	*P* = 1.000
	192 × 192	160 × 160	*P* = 1.000
Slice thickness (mm)			
	17	13	*P* = 0.280
	17	10	*P* = 0.068
	17	7	*P* = 0.068
	17	3	***P* = 0.000**
	13	10	*P* = 1.000
	13	7	*P* = 1.000
	13	3	*P* = 0.425
	10	7	*P* = 1.000
	10	3	*P* = 1.000
	7	3	*P* = 1.000

[1]Friedman test, *P* values of post-hoc testing including Bonferroni multiple testing correction; Hz, Hertz.

Supplementary Table 5. Pairwise comparisons of the artifact diameters at the tip (ball-like tip artifact) at various sequence parameters depending on the intervention angle

	Sample 1	Sample 2	
Parameter			***P* value**[1]
Intervention angle (°)			
	30	45	$P = 1.000$
	30	15	$P = 1.000$
	30	0	$\mathbf{P = 0.041}$
	45	15	$P = 1.000$
	45	0	$\mathbf{P = 0.047}$
	15	0	$P = 0.270$

[1]Kruskal–Wallis test, *P* values of post-hoc testing including Bonferroni multiple testing correction.

Supplementary Table 6. Quantitative assessment of contrast-enhanced target lesion to non-enhanced muscle tissue contrast ratio (*R*)

	$SI_{contrast\text{-}enhanced\ target\ lesion}$	$SI_{non\text{-}enhanced\ muscle\ tissue}$	R	
Parameter				***P* value**
Flip angle (°)				$P < 0.001$[1]
10	199.00	154.00	1.29	
20	350.00	246.00	1.42	
30	437.00	273.00	1.60	
40	479.00	259.00	1.85	
50	487.00	235.00	2.07	
60	533.00	154.00	2.29	
Bandwidth (Hz/pixel)				$P = 0.171$[1]
930	528.00	238.00	2.22	
1149	535.00	232.00	2.31	
1395	537.00	225.00	2.39	
1698	536.00	227.00	2.36	
Matrix (voxels)				$P = 0.003$[1]
96 × 96	489.00	246.00	1.99	
128 × 128	484.00	238.00	2.03	
160 × 160	515.00	219.00	2.35	
192 × 192	518.00	216.00	2.40	
224 × 224	584.00	200.00	2.92	
256 × 256	565.00	197.00	2.87	
Slice thickness (mm)				$P = 0.007$[1]
3	633.00	284.00	2.23	
7	564.00	260.00	2.17	
10	486.00	233.00	2.09	
13	449.00	215.00	2.09	
16	421.00	205.00	2.05	
Read-out direction				
RL	484.00	229.00	2.11	
AP	485.00	226.00	2.15	

This ratio was defined in terms of the following formula based on the mean SIs in the ROIs: $R = SI_{contrast\text{-}enhanced\ target\ lesion} / SI_{non\text{-}enhanced\ muscle\ tissue}$. To assess the corresponding signal intensities, defined ROIs of least 5 mm^2 were used. [1]Bravais–Pearson correlation coefficient; SI, signal intensity; ROI, region of interest; R: right; L, left.

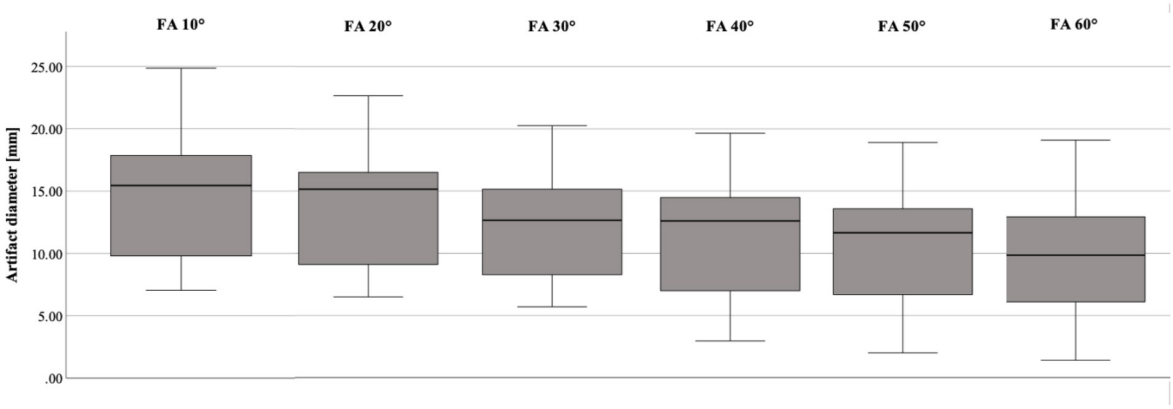

Supplementary Figure 1. Boxplots showing minimum, first quartile, median, third quartile, and maximum for artifact diameter size behavior as a function of the FA (10°–60°) averaged over all intervention angles. Note the gradually decreasing artifact size with the increase in FA ($P < 0.001$). FA, flip angle.

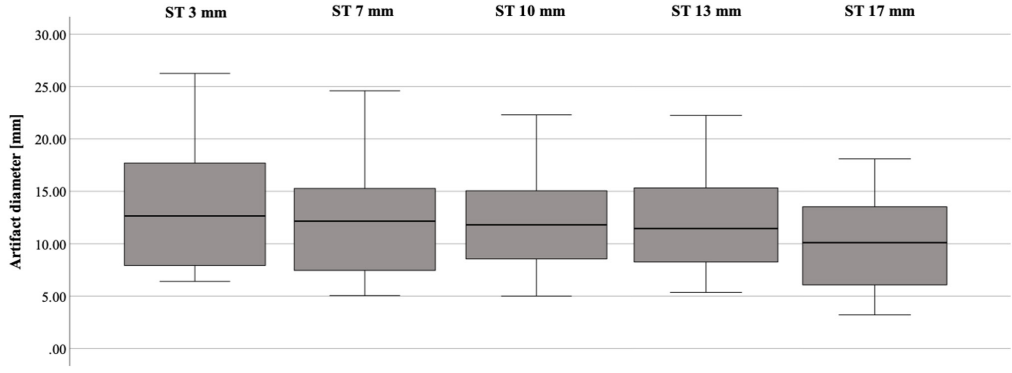

Supplementary Figure 2. Boxplots showing minimum, first quartile, median, third quartile, and maximum for artifact diameter size behavior as a function of the slice thickness (ST) (3–17 mm) averaged over all intervention angles. Note the significant differences in artifact size with the increase in ST ($P < 0.001$).